Research Article | Vol. 16, No. 10 / 1 Oct 2025 / Biomedical Optics Express 3923

Biomedical Optics EXPRESS

Optical diagnostics of liver tumors using an autofluorescence lifetime probe

Dafne Suraci,[1,*] Luca Tirloni,[2] Chiara Gatto,[2] Serena Pillozzi,[3] Lorenzo Antonuzzo,[4,5] Antonio Taddei,[2,5] and Riccardo Cicchi[1,6]

[1]*National Institute of Optics, National Research Council (INO-CNR), 50019, Sesto Fiorentino, Italy*
[2]*Hepatobiliopancreatic Surgery, Careggi University Hospital, 50134, Florence, Italy*
[3]*Department of Experimental and Clinical Biomedical Sciences 'Mario Serio', University of Florence, Firenze, Italy*
[4]*Clinical Oncology Unit, Careggi University Hospital, 50134, Florence, Italy*
[5]*Department of Experimental Clinical Medicine, University of Florence, 50134, Florence, Italy*
[6]*European Laboratory for Non-linear Spectroscopy (LENS), 50019, Sesto Fiorentino, Italy*
[*]*dafne.suraci@ino.cnr.it*

Abstract: Liver cancer is a global health challenge and its incidence is expected to grow worldwide to 1 million new cases in 2025. While hepatocellular carcinoma (HCC) is the most common liver cancer, hepatic metastases of colorectal cancer (CRLM) occur in almost 50% of patients with CRC. For both HCC and CRLM, surgical resection represents the only chance of long-term survival. In this context, a label-free optical surgical guidance tool would be highly suitable for reducing the positive margin rate and improving patient outcomes. In this study, we used a fiber-based autofluorescence lifetime imaging probe to provide real-time discrimination of tumor from marginal tissues in freshly excised liver samples. The proposed method allowed discriminating tumors from healthy tissue by reporting the fluorescence lifetime decay of cellular metabolic biomarkers, i.e., NAD(P)H and FAD. The acquisitions on 37 surgical specimens of both HCC and CRLM demonstrate that this approach is a method for delineating tumor borders with 67.7% and 77% accuracy, respectively. The results, combined with the ability to capture and process images in real time under bright background, highlight the technology's potential for clinical use for both label-free tissue diagnostics and surgical guidance.

1. Introduction

Hepatic cancers encompass a variety of liver malignancies, with the most prevalent of these being hepatocellular carcinoma (HCC) and cholangiocarcinoma (CCA). HCC accounts for approximately 75-85% of primary liver cancers and often develops in patients with underlying chronic liver conditions, including hepatitis B and C infections, alcohol-induced cirrhosis, and non-alcoholic fatty liver disease [1]. Though less common, CCA is an aggressive cancer originating from the biliary epithelium [2,3]. In addition to primary hepatic cancers, the liver is a frequent site of metastasis for other malignancies, most notably colorectal cancer (CRC). This is largely due to the liver's anatomical connection to the portal venous system, which drains blood from the gastrointestinal tract. Approximately 50% of CRC patients will develop liver metastases at some point [4,5] and, for most of them, liver represents the primary or sole site of metastatic involvement. The management of hepatic primary cancers or colorectal cancer liver metastases (CRLM) is a complex and evolving field. Significant advances have been made in surgical techniques, systemic chemotherapy, and targeted therapies, which have led to improved outcomes for many patients. Surgical resection of liver lesions, when feasible, is associated with significantly improved survival rates [6,7], with some studies reporting five-year survival rates of 25-40% for resected patients [8–10]. For those with unresectable lesions, systemic chemotherapy

#572468 https://doi.org/10.1364/BOE.572468
Journal © 2025 Received 3 Jul 2025; revised 23 Jul 2025; accepted 23 Jul 2025; published 4 Sep 2025

Biomedical Optics EXPRESS

and locoregional treatments such as radiofrequency ablation and trans arterial chemoembolization offer palliative benefits and may occasionally result in downstaging of tumors to a resectable status. However, despite advancements in therapeutic modalities, the accurate delineation of tumor margins and tumor progression in a surgical environment remains a key challenge, as medical imaging is generally performed pre-surgically. This underscores the need for novel imaging technologies that can enhance real-time tumor visualization, enabling both precise surgical interventions and improved diagnostic accuracy. In recent years, fluorescence lifetime imaging (FLIM) has emerged as a powerful tool for tissue characterization, offering label-free, non-invasive imaging based on the measurement of the fluorescence dynamic properties of biological molecules. Specifically, FLIM allows the assessment of key metabolic coenzymes such as nicotinamide adenine dinucleotide, NAD(P)H and flavins (FAD, FMN), whose fluorescence lifetimes are indicative of the metabolic state of tissues [11–14]. This technique provides valuable insights into cellular metabolism, with NAD(P)H fluorescence lifetime measurements being deeply characterized in the literature [15–19]. Protein-bound NAD(P)H exhibits longer fluorescence lifetimes (1.5-6 ns) than free NAD(P)H (0.3-0.8 ns), allowing the differentiation between normal and pathological tissues based on their autofluorescence decay and the corresponding metabolic signatures.

Among the various methods for FLIM, time-correlated single photon counting (TCSPC) remains the "gold standard" for its exceptional temporal resolution, sensitivity, and ability to resolve complex fluorescence decay functions [20,21]. This technology has been widely applied in the imaging of NAD(P)H, flavins and collagens to map tumor boundaries without the need for exogenous markers, further demonstrating its potential in clinical diagnostics [22–25]. Independently from the detection scheme, FLIM has been successfully integrated into fiber-optic probes, enabling real-time *in situ* tissue diagnostics in various applications. In particular, FLIM-based fiber probes have been used to delineate cancer margins in head and neck tissues [26,27], brain [28] and gastrointestinal tumors [29,30]. Marcu and colleagues employed a fiber-optic FLIM system integrated within a surgical microscope, providing high-resolution, intraoperative imaging during neurosurgical procedures [11]. In a related development, a single-photon avalanche diode (SPAD) array was implemented in a multispectral autofluorescence lifetime (FL) imaging system and successfully employed to detect metabolic changes in articular cartilage and other tissue models [31]. More recently, it has been demonstrated the utility of a bimodal fiber-based system to achieve multidimensional imaging of both colorectal cancer and human skin tissue [32]. These advancements illustrate the growing versatility of fiber-based FLIM systems across a wide range of medical applications. In particular, the combination of FL imaging with real-time feedback capabilities holds great promise for improving diagnostic accuracy and guiding therapeutic interventions in clinical settings. In this study, we used a custom made, optical fiber-based FLIM system to delineate surgical margins in hepatic cancers. Specifically, we report on the discrimination and delineation of malignant against both perilesional and healthy tissues on a cohort of 37 surgical specimens encompassing both HCC and CRLM. The results demonstrate a clear distinction of tumor against both adjacent margin and healthy regions based on their respective FL. The distinct lifetime profiles of CRLM with respect to HCC highlight the diagnostic potential of the proposed approach, and the analysis of FL components revealed preliminary insights into metabolic shifts associated with tumor progression.

2. Materials and methods

2.1. Sample collection and preparation

The tissue samples were collected from patients undergoing liver tumor resection at the Hepatobiliopancreatic Surgery, Careggi University Hospital in the period between 2023 and 2024, with a particular focus on HCC and CRLM. The study cohort, comprising 46 patients with an average age of 69 years (range 17-87 years), was conducted following a protocol approved by the

Biomedical Optics EXPRESS

local Ethics Committee (Number 21913_bio). Written informed consent was obtained from all participants, and all procedures were conducted in accordance with the tenets of the Declaration of Helsinki. All surgical specimens were obtained from patients previously diagnosed with either HCC (n = 22) or CRLM (n = 24). These diagnoses were subsequently validated through histopathological analysis. Liver tissue samples exhibiting signs of cirrhosis, fibrosis, or other inflammatory conditions were included in the study and documented in the patient clinical information. Biopsies that were collected after a prolonged period of tissue ischemia, from necrotic tissue, or from patients with a diagnosis other than CRC metastases or HCC were excluded. Tumor lesions ranged in size from 10 mm to 100 mm, biopsies smaller than 10 mm were excluded. In total, 9 human samples were excluded. After excision, the surgical specimens were immediately transported to the laboratory and processed according to an established protocol, summarized as follows. The samples were washed in Dulbecco's phosphate-buffered saline (DPBS) to remove residual blood and tissue fragments, and maintained at 4°C throughout the experiment, with the exception of spectroscopic measurements, performed at room temperature. Autofluorescence data were collected within 30 minutes from excision, ensuring consistent photon counts. Each tissue sample was meticulously annotated to delineate three distinct regions: the tumor lesion, the perilesional tissue surrounding the lesion, and healthy tissue. Due to clinical constraints, the collection of corresponding healthy tissues was not feasible for all the examined cases. A preliminary macroscopic evaluation of malignant lesions was conducted by pathologists. Regions of interest (ROIs) were defined based on expert evaluation. Particular attention was given to the ROIs selection, with the aim of having ROIs of approximately the same size in all the three tissue types (Fig. 1). To ensure clarity and avoid ambiguity throughout the manuscript, we will refer to neoplasia as "tumor", the perilesional tissue as "margin" and the healthy tissue far away from the lesion as "healthy".

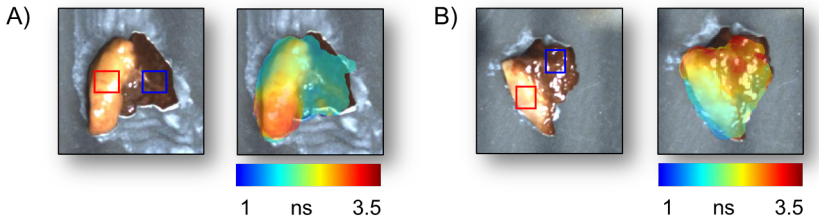

Fig. 1. Examples of a measurement on a liver HCC (A) and CRLM (B) showing: the white light image where the liver tissue is brown-red (blue ROI) and the cancer lesion is light brown (red ROI). The excised specimens are annotated by a pathologist defining two (margin and tumor) or three distinct tissue types (healthy, margin and tumor). The augmented-reality image of the FL is generated and superimposed to the white light image of the sample on the screen with FL data represented in a color-coded scale.

2.2. Autofluorescence lifetime (FL) instrumentation and acquisitions

FL measurements were conducted using a custom-made optical system, optimized for real-time tissue analysis and previously described in detail elsewhere [33]. Briefly, the system uses a picosecond pulsed laser diode emitting at 375 nm with a repetition rate of 20 MHz. The excitation light, along with a 660 nm aiming beam from a red LED (M660FP1, Thorlabs, Newton, NJ, USA), was delivered to the tissue under examination through a spliced fiber inserted in a trifurcated optical fiber bundle (FiberTech Optica, Montreal, Canada). The bundle consists of a central 400 µm diameter excitation fiber and nine 200 µm diameter collection fibers arranged concentrically, enabling effective collection of the autofluorescence signal. This bundle was

Biomedical Optics EXPRESS

handheld and moved across the specimen for scanning. The collected signal was filtered using emission filters (FF01-470/28-25 and FF01-534/20-25, Semrock, Rochester, NY, USA) to maximize detection of key endogenous fluorophores, respectively NAD(P)H to the 470 ± 14 nm band (CH1) and flavins predominantly in the 534 ± 10 nm band (CH2) and was detected by a high-sensitivity hybrid detector (HPM-100-40, Becker & Hickl GmbH). A time-correlated single photon counting (TCSPC) acquisition card (SPC-730, Becker & Hickl GmbH) was employed to record fluorescence intensity decays from each channel alternatively, upon changing of the corresponding fluorescence filter. This setup allowed reconstructing of spatially resolved FL maps from single-point measurements. The handheld fiber probe was moved freely over the tissue surface, and the aiming beam provided a visual reference for guiding data acquisition and for tracking the position [33]. A USB camera, with resolution of 640 × 480 pixels (DFK33UP1300, The Imaging Source, Bremen, Germany), is synchronized with a white LED that provides uniform illumination and used for tracking the position of the aiming beam across the specimen. Following the image acquisition, each captured frame is processed for identification of the guiding beam position (detecting the 660 nm beam). These data are then merged with fluorescence lifetime data to generate augmented maps that are displayed to the user in real-time. During the measurements the probe was kept as close as possible to the sample surface, with the laser power maintained around 10 μW of average power. Optical measurements were completed within a total time of 5 minutes, with the entire sample surface mapped in less than a minute.

2.3. Phasors-based and fit-based analyses

FL data were analyzed using the phasor approach, a fit-free method that transforms fluorescence decay data into a two-dimensional phasor plot upon Fourier transform, allowing for rapid visualization of lifetime characteristics. Single-exponential decays are mapped into a point located along the universal circle, while mixtures of fluorophores are mapped within this circle, representing an average of their individual lifetimes. The phase lifetime (τ_{phase}) is calculated from the g and s coordinates of the phasor plot. This method is ideal for real-time applications due to its fast-processing capabilities and has been extensively validated in the literature for its ability to resolve complex decay profiles [34–36]. In brief it employs the Fourier transformation of the fluorescence intensity decay to produce Real and Imaginary components $g(\omega)$ and $s(\omega)$, respectively, where $\omega = 2\pi f$ is the angular frequency related to the laser repetition rate (f), i.e. 20 MHz. The instrument response function (IRF) was measured using back reflected excitation light from a reflective surface and the signal used as reference phasor. Measured τ_{phase} was calculated as follows per each decay curve:

$$\tau_{phase} = \frac{1}{\omega}\frac{s_{measured}}{g_{measured}} - \tau_{IRF} \tag{1}$$

System response de-convolution and fluorescence decay analysis were performed using custom LabVIEW software, which also provided real-time augmented reality overlays of fluorescence lifetime maps on white-light images [29,37]. Image processing, data visualization and classification methods were supported by MATLAB (R2022b, The MathWorks, Inc., USA). Acquisitions with photon counts lower than 100 per decay were discarded to ensure uniformity in the analysis by thresholding the SNR.

Additional data analysis was performed fitting fluorescence decay data to a double-exponential decay function:

$$I_{measured}(t) = \mathrm{IRF}(t) * (\alpha_1 e^{-t/\tau_1} + \alpha_2 e^{-t/\tau_2}) + C \tag{2}$$

where a_1, a_2 and τ_1, τ_2 are the pre-exponential factors and fluorescence lifetimes of the fast and slow components of the fluorescence intensity decay, respectively. A double-exponential, rather than a three-exponential, fit function was chosen due to the limited number of photons available at the peak (few hundreds), using this specific optical scheme and integration time, in order to avoid

Biomedical Optics EXPRESS

data overfitting. This allowed extracting the short and long fluorescence lifetime components and their a_1/a_2 ratio, that is informative about cellular metabolic profile. In fact, for NAD(P)H autofluorescence decay, the two lifetime components are related to the free and protein-bound fraction of NAD(P)H. The a_1 component is related to the relative abundance of free NAD(P)H, while a_2 to the protein-bound form [38]. In this study, we used the a_1/a_2 parameter to highlight the metabolic changes occurring in the tumor as compared to the corresponding healthy tissue. I.e., a proliferative state as in tumor cells generally has a metabolic profile unbalanced towards glycolysis, with an increased amount of metabolic cofactor NAD(P)H. The same metrics of analysis have been consistently applied to both detection channels.

2.4. Statistical analysis

Surgical margin assessed during surgery was used as reference to determine tumor position with respect to the healthy margin and evaluate differences between groups following the FLIM measurements. Two or three regions of interest (ROIs: tumor, margin, healthy) were extracted per each surgical specimen and the FL data used for further statistical analysis. Data were primary divided per patient diagnosis, HCC or CRLM. FL data are represented as mean τ_{phase} calculated per each ROI depicted for individual patient's specimen. Those values are represented divided into the three ROIs as dots contained within the half box. Box plots are used to show the data distribution within the equal tissue in different specimens. The horizontal line within the box indicates the median of the distribution across patients. The box spans the interquartile range (IQR) and the whiskers extend to values within the IQR, identifying the range of non-outlier observations. Parametric data underwent analysis using paired t-test. A 95% confidence interval was applied, ensuring a reliable assessment of relationships and differences in the study variables.

The probability value of $p < 0.05$ was considered significant. We quantified the spread of data within each ROI through the coefficient of variation (CV), calculated as the ratio between standard deviation (SD) and mean. The CV measures the relative variability of a set of data points with respect to their mean, providing a normalized measure that facilitates comparison of the degree of dispersion across different datasets. A larger CV indicates greater relative variability within a set of data. The relative difference between the mean FL values for each tissue type was calculated as:

$$\Delta\tau = \frac{\tau_k - \tau_z}{\tau_z} \tag{3}$$

where, τ_k refers to the FL of the region of interest (e.g., tumor or margin), and τ_z represents the reference region (e.g., margin or healthy tissue, respectively). The same calculation was performed to highlight the relative differences between the a_1/a_2 ratio following this Eq:

$$\Delta(a_1/a_2) = \frac{(a_1/a_2)_k - (a_1/a_2)_z}{(a_1/a_2)_z} \tag{4}$$

The subscripts k and z are consistent with those previously defined for the calculation of $\Delta\tau$, where k represents the region of interest (e.g., tumor or margin) and z refers to the reference region (e.g., margin or healthy tissue). This approach ensures a consistent framework for comparing the fluorescence behavior across different tissue types. All statistical analyses, graphs, and histograms were conducted and realized using Microcal Origin Pro 8.0 (OriginLab Corporation, Northampton, MA, US) and GraphPad Prism software.

3. Results

3.1. Analysis of liver metastases of colorectal cancer (CRLM)

The suitability of our system to report endogenous contrast from freshly resected gastrointestinal surgical specimens in a relevant clinical setting was already demonstrated elsewhere [29]. Here

Biomedical Optics EXPRESS

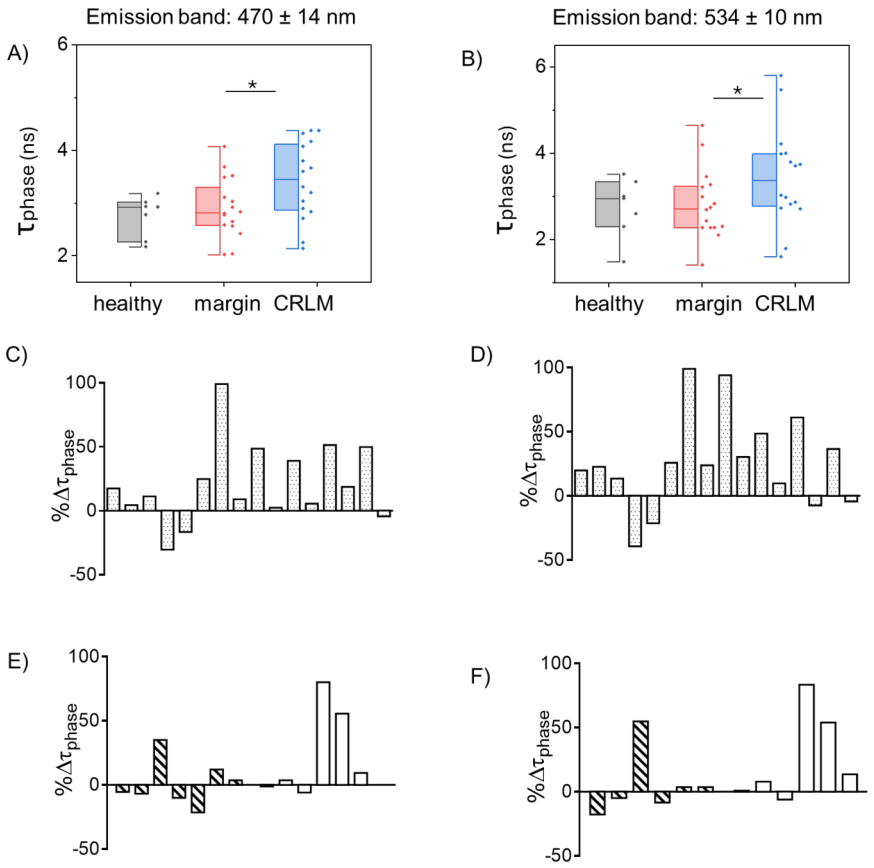

Fig. 2. FL (τ_{phase}) measurements in 16 CRLM cases. A) Distributions of mean autofluorescence lifetimes for healthy (grey), margin (red), and tumor (light blue) regions in CH1 from freshly excised specimens. B) Distributions of mean FLs for healthy (grey), margin (red), and tumor (light blue) regions in CH2. The percentage difference in FL between tumor and margin tissues $\Delta\tau$ is displayed in C) and D) for CH1 and CH2, respectively. Cases are reported in order from patient n. 1 to 16th, in accordance with Table S1. E) and F) show $\Delta\tau$ comparisons between margin and healthy tissues (black lines pattern), as well as between tumor and healthy tissues (white barrs), for CH1 and CH2, respectively. Paired tests were applied to determine p-values, with $p < 0.05$.

we report the results obtained on a cohort of 37 surgical specimens encompassing both HCC and CRLM. More in detail, CRLM lesions are characterized by a light brown color with a characteristic cellular exudate, providing significant morphological contrast against the dark brown colored marginal tissue in its proximity, which was immediately identified by clinical eye at the time of the resection (Fig. S1).

Tumor and normal tissues were later identified in all lesions by histopathological exam (Table S1). A number of tumor and margin specimens (n = 7) were sampled together with a healthy liver fragment from the same patient. From the initial cohort of 24 selected patients with CRLM, a final set of 16 samples were included in the analysis based on the inclusion/exclusion criteria summarized in the methods section. The statistical analyses including the 16 selected cases are presented in Fig. 2. Tumor and surgical margin can be clearly identified by the FL data (Fig. 2 A and B). Both margin and healthy tissue yield shorter FLs in comparison with tumor

Biomedical Optics EXPRESS

tissue. Similar differences were found in both detection channels. The differences are statistically significant, with a p value equal to 0.0231 for CH 1 (Fig. 2A) and to 0.0336 for CH 2 (Fig. 2D). The mean τ_{phase} for our cohort of 16 CRLM collected specimens, was found equal to 3.4 ± 1.0 ns on both spectral channels, compared to a value of 2.9 ± 0.5 ns for both margin and healthy tissue in CH 1, whereas in CH 2 the values were 2.8 ± 0.8 ns for margin and 2.7 ± 0.6 ns for healthy tissue. See Table 2 for detailed mean FL values. The CRLM was detected with a sensitivity of 82% and a specificity of 72% (Fig. S2). Despite the significant difference among lifetime values on both spectral channels, an interesting outcome is represented by the distribution of lifetime data, which is significantly broader in tumor with respect to the other tissue types, probably due to a larger inter patient variability.

To mitigate the potential bias introduced in our analysis by inter patient variability, relative difference values were calculated between CRLM and margin within the same measurements. Analysis of relative values allowed us to visualize specific patterns in the optical data. The notation used is described in Eq. (3). In this analysis, only paired measurements from specimens with both margin and tumor regions were considered. The $\Delta\tau$ values (Figs. 2C and 2D) indicated a positive difference for CRLM relative to the margin tissue, thereby revealing a distinct fluorescence lifetime profile for the tumor. In contrast, only three cases (in CH1) and four cases (in CH2) of CRLM exhibited a negative difference with respect to the corresponding margin. In Fig. 2E and 2F are reported the differences in the $\Delta\tau$ between healthy tissue and its paired margin, or between healthy and CRLM tissue (Eq. (3)). Although this comparison was feasible only for a small subset, the data consistently demonstrated a characteristic behavior of CRLM compared to healthy tissue. On the other hand, the comparison between healthy and margin exhibited discernible disparities, though these remained below 50%.This finding agrees with the assumption that resected areas around CRLM (margin), likely exhibit a metabolic profile comparable to healthy regions.

The FL data across ROIs demonstrated a broad distribution of τ_{phase} within the sampled liver tissues. Both margins and CRLM lesions showed substantial inter-patient variability. Specifically, coefficients of variation (CV) for tumor tissues were 0.22 in CH1 and 0.33 in CH2, while margin showed CVs of 0.20 in CH1 and 0.29 in CH2. In comparison, healthy tissues ($n = 7$) showed lower variability, with CVs of 0.14 in CH1 and 0.25 in CH2. The differences in CVs between CRLM and margin are modest, showing a greater heterogeneity within those regions with respect to healthy regions.

3.2. Analysis of hepatocellular carcinoma (HCC)

HCC is a primary liver tumor that can present various degrees of differentiation and progression. Of the initial cohort of 22 HCC patients selected for sampling, 19 samples ultimately met the clinical or experimental inclusion criteria and were included in the subsequent analysis. The HCC samples included in the study were grouped based on the Edmonson differentiation from grade 1 to grade 3, resulting in a total of 4 cases with grade 1, 11 cases with grade 2 and 3 cases with grade 3. In patients affected by HCC often a pre-event of liver inflammation or cirrhosis was present. Five patients presented cirrhosis, while 10 presented fibrosis (Table S2). The FL data across ROIs demonstrated a broad distribution of τ_{phase}, where both margins and HCC exhibited considerable inter-patient variability (Fig. 3A and 3B) . The variability grade observed resulted in a lack of a well-defined autofluorescence signature across the cohort. In general, HCC cases showed greater heterogeneity among patients, with a sensitivity of 65% and a specificity of 71% in detecting the margin relative to the tumour (Fig S2). In particular, the CV for tumor samples were 0.32 and 0.42 in CH1 and CH2, respectively. In contrast, margin tissue exhibited a CV of 0.26 in CH1 and 0.31 in CH2. The healthy tissue, which was collected from only a subset of patients ($n = 5$), demonstrated lower inter-patient variability, with a CV of 0.13 in CH1 and 0.22 in CH2. Notably, all cases of healthy tissue displayed mild portal fibrosis while remaining otherwise normal. Only one case presented with cirrhosis, which exhibited the highest τ_{phase}

Biomedical Optics EXPRESS

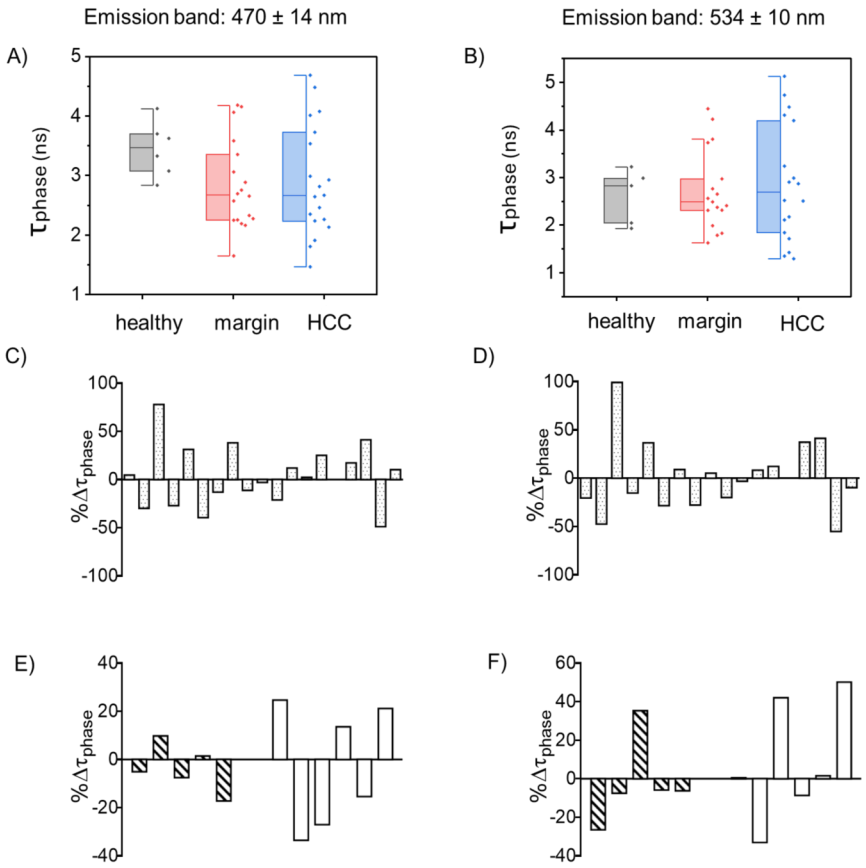

Fig. 3. FL (τ_{phase}) measurements in 19 distinct HCC cases. A) Distributions of mean autofluorescence lifetimes for healthy (grey), margin (red), and tumor (light blue) regions in CH1 from freshly excised specimens. B) Distributions of mean FLs for healthy (grey), margin (red), and tumor (light blue) regions in CH2. The percentage difference in FL between tumor and margin tissues $\Delta\tau$ is displayed in C) and D) for CH1 and CH2, respectively. Cases are reported in order from patient n. 1 to 19, in accordance with Table S2. E) and F) show $\Delta\tau$ comparisons between margin and healthy tissues (black-line pattern bars), as well as between HCC and healthy tissues (white bars), for CH1 and CH2, respectively. Paired tests were used to calculate p-values, with no significant differences observed.

among all cases (τ_{phase} = 4.0 ns). Pairwise comparisons of mean τ_{phase} values between different regions of each sample did not reveal statistically significant variations. In particular, we did not find any significant difference between HCC and margin tissue when considering absolute τ_{phase} values. Further analysis of the $\Delta\tau$, (Eq 3) between HCC and their corresponding margin, revealed two distinct patterns (Fig. 3C and 3D). The first pattern exhibited a positive $\Delta\tau$, with HCC lesions having a longer lifetime than marginal tissues. In contrast, the second pattern demonstrated a negative $\Delta\tau$, whereby the margin tissues exhibited a longer τ_{phase} than the tumor lesions (Fig. S1). These two distinct $\Delta\tau$ behaviors demonstrate consistent values and similar distributions across both channels (Fig. 3E and 3F). In particular, the mean τ_{phase} for margin tissue ranges from 2.6 ns in CH1 and 2.8 ns in CH2, up to a maximum of 3.0 ns in both channels. In contrast, regions of HCC display shorter mean τ_{phase} values, ranging from 2.3 ns to a maximum of 3.6 ns in CH1 and 3.5 ns in CH2. Detailed values with SD are reported in Table 1 and Table S3. Statistically

Biomedical Optics EXPRESS

significant differences between HCC and peripheral tissues were evaluated when analyzed in separated groups based on positive or negative $\Delta\tau$ values, with a p-value < 0.05 (Table S3). The present analysis, in conjunction with the distinct patterns highlighted therein, underscores the complexity of interpreting FL data from a physiological point of view.

Table 1. Autofluorescence lifetime mean values and decay components ratio

	HCC			CRLM		
Tissue	normal	margin	tumor	normal	margin	tumor
τ_{phase} CH1	3.4 ± 0.4	2.8 ± 0.7	2.9 ± 0.9	2.9 ± 0.6	2.9 ± 0.5	3.4 ± 0.7
τ_{phase} CH2	2.6 ± 0.5	2.7 ± 0.8	2.9 ± 1.2	2.7 ± 0.6	2.8 ± 0.8	3.4 ± 1.1
a_1/a_2 CH1	0.35 ± 0.1	0.30 ± 0.1	0.27 ± 0.1	0.30 ± 0.1	0.40 ± 0.1	0.30 ± 0.1
a_1/a_2 CH2	0.40 ± 0.05	0.35 ± 0.1	0.30 ± 0.1	0.20 ± 0.1	0.30 ± 0.1	0.25 ± 0.1

3.3. *Autofluorescence lifetime component a_1/a_2*

The analysis of the autofluorescence decay components revealed a lower value of the a_1/a_2 ratio for both CRLM and HCC lesions when compared to their corresponding margins, as shown in Fig. 4, indicating a lower a_1/a_2 ratio within tumor cells. Tumor cells can exhibit a highly proliferative metabolism, which is often accompanied by metabolic dysregulation due to genetic mutations and deregulated cellular functions. The observed reduced a_1/a_2 ratio in both examined lesions is likely associated with an increased presence of protein-bound NAD(P)H, as reflected in CH1 (predominantly NADH) and CH2 (a mixture of NADH and flavins). The a_1 component reflects the fraction of free NAD(P)H, while the a_2 component is associated with NAD(P)H bound to enzymatic proteins, such as those involved in oxidative phosphorylation (OXPHOS). A higher a_1/a_2 ratio indicates a greater proportion of free NAD(P)H, which is often linked to increased glycolytic activity—a feature commonly seen in more aggressive tumors [39]. This parameter is important to delineate a metabolic profile, that can provide insights on how a tumor might respond to certain treatments [40,41]. It is observed an increased a_1/a_2 ratio in tumor lesions compared to the adjacent margins in four cases of HCC. Notably, all these cases were classified as grade 2 HCC, except for one case, classified as a grade 2-3 tumor. Most of HCC in our cohort were grade 2, limiting the ability to draw direct conclusions about the relationship between tumor grade, autofluorescence and metabolic changes. However, our findings highlight the potential of the a_1/a_2 ratio to detect early metabolic switches early, particularly in tumor progression. This suggests the intriguing possibility that metabolic alterations could precede detectable structural changes in tumor cells. If the ratio shifts towards a lower value, it may indicate a transition in the tumor's metabolic state, potentially reflecting a response to treatment. Notably, inter-patient variability appears reduced in these data, suggesting a more defined metabolic signature across samples. A comparison of the a_1/a_2 ratio between HCC tumors and the paired margin showed a statistically significant lower a_1/a_2 ratio in the tumors (0.27 versus 0.30, $p = 0.023$) (Fig. 4). The CRLM cases presented a lower a_1/a_2 ratio with respect to the margin, 0.3 versus 0.4 ($p = 0.004$) in CH1, while the paired difference was not statistically significant in CH2.

Biomedical Optics EXPRESS

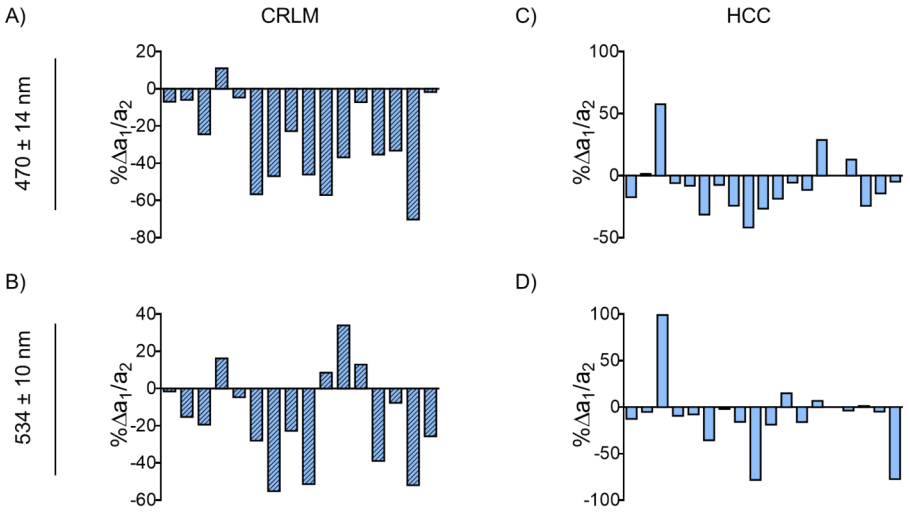

Fig. 4. Relative variation, measured with respect to the mean value, of the FL components ratio between: CRLM lesions and their corresponding margins in CH1 (A) and CH2 (B); HCC lesions and their corresponding margins in CH1 (C) and CH2 (D). Cases are reported in order with patient numbers on Table S1 and S2.

4. Discussion

The ability of optical metabolic imaging to distinguish cancerous cells from normal cells has been widely investigated *in vitro* and *in vivo*, with particular attention to monitoring the cellular response to different metabolic conditions and its correlation with autofluorescence decay data. In cancer cells, a third hybrid metabolic phenotype has been described. This is characterized by increased enzymatic activity and concomitant activation of glycolysis and OXPHOS pathways. This gives the cells the ability to respond to microenvironment changes easily and to gain general survival advantages during tumor progression. This metabolic plasticity has been linked with metastasis and chemoresistance. The system described in this paper is designed to selectively probe the superficial layer of the hepatic epithelium, with an estimated penetration depth of approximately 100 µm. As a result, the autofluorescence signal primarily originates from fluorophores located near the tissue surface. In CH1, the dominant contribution is from NAD(P)H, whose emission peaks around 440-470 nm and which is abundantly present in metabolically active epithelial cells. Although other endogenous fluorophores can be excited at 375 nm, the emission filter is optimized to selectively capture NAD(P)H fluorescence and reduce potential spectral overlap. In CH2, the main contributors are flavins (such as FAD and FMN), which emit near 530 nm. While bilirubin and lipofuscin may also contribute to the signal in this region, their influence is expected to be minimal under the current acquisition conditions. NAD(P)H also contributes to the overall signal considering its excitation/emission spectra [16], but the overlap between flavin and NAD(P)H emission in CH2 must be considered for the interpretation of acquired data, as the two nucleotides provide complementary information. Given the shallow imaging depth, fluorophores localized in deeper hepatic structures, such as collagen or vitamin A, are unlikely to significantly affect the detected signal. Across the analyzed samples, a significant increase of fluorescence lifetime was observed in CRLM regions compared to both adjacent margin and healthy tissues on the two different detection channels.Comparative analysis of the biopsy or surgical cancer material and surrounding healthy tissue showed almost unchanged glycolytic activity and upregulation of OXPHOS in CRC [42]. The CRC cells demonstrate a metabolic shift towards OXPHOS, which is likely to facilitate cell proliferation and migration. In our cohort of

Biomedical Optics EXPRESS

CRLM samples, the observed FL features agree with a cofactors-mediated upregulated oxidative metabolism and cellular stress responses. Additionally, the uniformity in longer fluorescence lifetimes across the CRLM samples, confirmed by a quantified low inter-patient variability (CV), suggests that this may represent a CRC metastatic metabolic signature, potentially facilitating their identification during surgical procedures.

A number of studies report that HCC cells typically undergo metabolic reprogramming characterized by enhanced glycolysis, fatty acid synthesis, and glutamine metabolism [43,44]. Metabolic phenotypes in HCC are heterogeneous and can vary with tumor grade, microenvironment, and underlying liver pathology. The distinction between tumor tissues with longer or shorter τ_{phase} values may indicate two distinct metabolic states, allowing us to infer metabolic positioning even among HCC samples of the same grade (e.g., grade 2). The statistically significant differences observed in $\Delta\tau$ values between margin and tumor tissues ($p < 0.01$) indicate the potential for two distinct metabolic behaviors that co-exist within HCC samples (Fig. S1, Table S3).

Further, the ratio of the amplitudes of the fluorescence lifetime components a_1/a_2 suggests a shift towards a more OXPHOS-dominant metabolic signature in our HCC samples. This information could be crucial for identifying metabolic vulnerabilities and adapting treatment strategies based on the tumor's metabolic profile, especially when combined with the analysis of other decay components. It has been observed a higher a_1/a_2 ratio in tumor lesions compared to adjacent margins in 4 out of 19 cases of HCC. Most of HCCs in our cohort were grade 2, limiting the ability to draw direct conclusions about the relationship between tumor grade and metabolic changes. However, our findings highlight the potential of the a_1/a_2 ratio to detect early metabolic shifts, particularly in the progression from grade 2 to grade 3. All the observed cases were classified as grade 2 HCC, except for one case, classified as a grade 2-3. Given the prevalence of grade 2 cases, a larger sample size and more comprehensive clinical data are necessary to more accurately assess this relationship. These findings indicate the potential of the a_1/a_2 ratio to be used as an early biomarker for the metabolic switch associated with tumor progression from grade 2 to grade 3.

Although a direct correlation with histopathological results is difficult to be performed, as histological images are inherently sagittal, while our images contain information only from tissue surface, the obtained results demonstrate that autofluorescence lifetime can represent a valid diagnostic support at the clinical level, providing significant advantage with respect to the state-of-the-art in the field. In fact, the standard medical imaging modalities such as Computed Tomography (CT), Magnetic Resonance Imaging (MRI), and Positron Emission Tomography (PET), provide an important imaging reference to the clinicians but they are performed only pre-operatively. In this scenario, autofluorescence lifetime imaging may represent a valid imaging support during surgery procedures by providing a needed image-based guidance for the clinicians. Nevertheless, a significant amount of work needs to be done before translating such approach from a research method in a recognized clinical standard. Compared to other emerging imaging technologies for clinical diagnostics, such as Stimulated Raman Scattering (SRS) and Optical Coherence Tomography (OCT), our method offers advantages and drawbacks. SRS provides a more detailed molecular characterization than fluorescence lifetime but is less flexible, as it is generally implemented using a microscopic approach that requires imaging of a resected biopsy specimen to provide a rapid intrasurgical diagnostics rather than for intravital imaging. OCT offers the advantage of being already a standard clinical modality that can be implemented within optical fibers, but it is limited to morphological information, without providing functional or metabolic information. Both SRS and OCT can provide micron-scale spatial resolution and deep imaging capability compared to our approach that is superficial and with a spatial resolution in the mm-range. Despite this limitation, considering that tumor resection is performed using a bisturi or a similar device, the resolution offered by our method perfectly matches the resolution achievable during surgical resection. Despite the limitations and the significant work to be done

Biomedical Optics EXPRESS

for translating this technology to the clinical scenario, we believe that autofluorescence lifetime imaging can represent a valid support for surgical guidance.

5. Conclusion

The results of our study indicate that our fiber-based FL imaging approach is a method for distinguishing and delineating tumor from non-tumor regions, as well as to highlight lesion-specific patterns. This suggests the potential for establishing specific fluorescence lifetime signatures for CRLM and HCC. Nevertheless, a larger sample size is necessary to comprehensively define these lifetime characteristics and evaluate their correlation with key clinical parameters. Such factors include previous treatments (e.g. chemotherapy, radiotherapy), levels of tumor differentiation, and disease progression within the liver, each of them having the potential to significantly influence the metabolic landscape and autofluorescence response of the tissue. These insights indicate that FL imaging has the potential to be used not only as an intraoperative tool to accurately define resection margins, but also as a diagnostic modality suitable for both *in vivo* and *ex vivo* applications. This approach could support a more dynamic assessment of tissue status and potentially allow real-time evaluation of tissue metabolic characteristics for personalized surgical and treatment decisions based on the unique autofluorescence profiles of different tumor types.

Funding. Co-funded by the European Union NextGenerationEU, program PRIN 2022 (grant number 2022Y9YP9C ALIAS); Co-funded by the European Union under HEU-GA (101131771 Lasers4EU).

Acknowledgments. The authors thank all personnel of the Hepatobiliopancreatic Surgery team at Careggi Hospital for their involvement in sample collection and their assistance with sample information. Special thanks go to Dr Enrico Baria for his support with the classification analysis.

Views and opinions expressed are however those of the author(s) only and do not necessarily reflect those of the European Union. The European Union cannot be held responsible for them.

Disclosures. The authors declare no conflicts of interest.

Data availability. The data that support the findings of this study are available from the authors upon request.

Supplemental document. See Supplement 1 for supporting content.

References

1. A. Forner, M. Reig, and J. Bruix, "Hepatocellular carcinoma," Lancet **391**(10127), 1301–1314 (2018).
2. S. A. Khan, S. Tavolari, and G. Brandi, "Cholangiocarcinoma: Epidemiology and risk factors," Liver Int. **39**(S1), 19–31 (2019).
3. R. El-Diwany, T. M. Pawlik, and A. Ejaz, "Intrahepatic cholangiocarcinoma," Surg Oncol Clin N Am **28**(4), 587–599 (2019).
4. M. Arnold, M. S. Sierra, M. Laversanne, *et al.*, "Global patterns and trends in colorectal cancer incidence and mortality," Gut **66**(4), 683–691 (2017).
5. J. Scheele, R. Stangl, and A. Altendorf-Hofmann, "Hepatic metastases from colorectal carcinoma: Impact of surgical resection on the natural history," Br. J. Surg. **77**(11), 1241–1246 (1990).
6. D. Archampong, D. Borowski, P. Wille-Jørgensen, *et al.*, "Workload and surgeoṅs specialty for outcome after colorectal cancer surgery," Cochrane Database of Systematic Reviews **2012**(3), CD005391 (2012).
7. D. A. Ahlquist, H. Zou, M. Domanico, *et al.*, "Next-generation stool DNA test accurately detects colorectal cancer and large adenomas," Gastroenterology **142**(2), 248–256 (2012).
8. Z. Pan, J. Peng, J. Lin, *et al.*, "Is there a survival benefit from adjuvant chemotherapy for patients with liver oligometastases from colorectal cancer after curative resection?" Cancer Commun **38**(1), 1–10 (2018).
9. P. Scherman, P. Hansdotter, E. Holmberg, *et al.*, "High resection rates of colorectal liver metastases after standardized follow-up and multimodal management: an outcome study within the COLOFOL trial," Hpb **25**(7), 766–774 (2023).
10. L. Bernier, S. Balyasnikova, D. Tait, *et al.*, "Watch-and-wait as a therapeutic strategy in rectal cancer," Curr Colorectal Cancer Rep **14**(2), 37–55 (2018).
11. A. Alfonso-Garcia, J. Bec, S. Sridharan Weaver, *et al.*, "Real-time augmented reality for delineation of surgical margins during neurosurgery using autofluorescence lifetime contrast," J Biophotonics **13**(1), 1–12 (2020).
12. J. Unger, C. Hebisch, J. E. Phipps, *et al.*, "Real-time diagnosis and visualization of tumor margins in excised breast specimens using fluorescence lifetime imaging and machine learning," Biomed. Opt. Express **11**(3), 1216 (2020).
13. A. Alfonso-Garcia, S. N. Anbunesan, J. Bec, *et al.*, "In vivo characterization of the human glioblastoma infiltrative edge with label-free intraoperative fluorescence lifetime imaging," Biomed. Opt. Express **14**(5), 2196 (2023).
14. S. Kalinina, J. Breymayer, P. Schäfer, *et al.*, "Correlative NAD(P)H-FLIM and oxygen sensing-PLIM for metabolic mapping," J Biophotonics **9**(8), 800–811 (2016).

Biomedical Optics EXPRESS

15. M. C. Skala, K. M. Riching, D. K. Bird, *et al.*, "In vivo multiphoton fluorescence lifetime imaging of protein-bound and free nicotinamide adenine dinucleotide in normal and precancerous epithelia," J. Biomed. Opt. **12**(2), 024014 (2007).
16. M. Y. Berezin and S. Achilefu, "Fluorescence lifetime measurements and biological imaging," Chem. Rev. **110**(5), 2641–2684 (2010).
17. T. S. Blacker and M. R. Duchen, "Investigating mitochondrial redox state using NADH and NADPH autofluorescence," Free Radical Biol. Med. **100**, 53–65 (2016).
18. O. I. Kolenc and K. P. Quinn, "Evaluating cell metabolism through autofluorescence imaging of NAD(P)H and FAD," Antioxid. Redox Signaling **30**(6), 875–889 (2019).
19. G. Papayan, N. Petrishchev, and M. Galagudza, "Autofluorescence spectroscopy for NADH and flavoproteins redox state monitoring in the isolated rat heart subjected to ischemia-reperfusion," Photodiagn. Photodyn. Ther. **11**(3), 400–408 (2014).
20. W. Becker, L. M. Hirvonen, J. Milnes, *et al.*, "A wide-field TCSPC FLIM system based on an MCP PMT with a delay-line anode," Rev. Sci. Instrum. **87**(9), 093710 (2016).
21. V. I. Shcheslavskiy, M. V. Shirmanova, A. Jelzow, *et al.*, "Multiparametric time-correlated single photon counting luminescence microscopy," Biochemistry (Moscow) **84**(S1), 51–68 (2019).
22. R. Cicchi, A. Crisci, A. Cosci, *et al.*, "Time- and Spectral-resolved two-photon imaging of healthy bladder mucosa and carcinoma in situ," Opt. Express **18**(4), 3840 (2010).
23. V. I. Shcheslavskiy, M. V. Shirmanova, V. V. Dudenkova, *et al.*, "Fluorescence time-resolved macroimaging," Opt. Lett. **43**(13), 3152 (2018).
24. A. Marcek Chorvatova, M. Cagalinec, and D. Chorvat, "Time-Resolved Imaging of Mitochondrial Flavin Fluorescence and Its Applications for Evaluating the Oxidative State in Living Cardiac Cells," Methods Mol Biol **2275**, 403–414 (2021).
25. J. Horilova, H. Studier, Z. Nadova, *et al.*, "Time-resolved spectrometry of mitochondrial NAD(P)H fluorescence and its applications for evaluating the oxidative state in living cells," Methods Mol Biol **1264**, 183–193 (2015).
26. M. A. Hassan, B. W. Weyers, J. Bec, *et al.*, "Anatomy-specific classification model using label-free FLIm to aid intraoperative surgical guidance of head and neck cancer," IEEE Trans. Biomed. Eng. **70**(10), 2863–2873 (2023).
27. B. W. Weyers, M. Marsden, T. Sun, *et al.*, "Fluorescence lifetime imaging for intraoperative cancer delineation in transoral robotic surgery," Transl. Biophotonics **1**(1-2), e201900017 (2019).
28. L. Marcu and B. A. Hartl, "Fluorescence lifetime spectroscopy and imaging in neurosurgery," IEEE J. Select. Topics Quantum Electron. **18**(4), 1465–1477 (2012).
29. D. Suraci, E. Baria, L. Tirloni, *et al.*, "Delineation of gastrointestinal tumors biopsies using a fluorescence lifetime imaging optical fiber probe," J Biophotonics **18**, e202400122 (2024).
30. E. V. Potapova, V. V. Shupletsov, V. V. Dremin, *et al.*, "In Vivo Time-Resolved Fluorescence Detection of Liver Cancer Supported by Machine Learning," Lasers Surg. Med. **56**(10), 836–844 (2024).
31. J. L. Lagarto, C. Credi, F. Villa, *et al.*, "Multispectral depth-resolved fluorescence lifetime spectroscopy using SPAD array detectors and fiber probes," Sensors (Switzerland) **19**(12), 2678 (2019).
32. A. I. Herrando, M. Castillo-Martin, A. Galzerano, *et al.*, "Dual excitation spectral autofluorescence lifetime and reflectance imaging for fast macroscopic characterization of tissues," Biomed Opt Express **15**(6), 3507 (2024).
33. J. L. Lagarto, V. Shcheslavskiy, F. S. Pavone, *et al.*, "Real-time fiber-based fluorescence lifetime imaging with synchronous external illumination: A new path for clinical translation," J Biophotonics **13**(3), e201960119 (2020).
34. P. H. Lakner, M. G. Monaghan, Y. Möller, *et al.*, "Applying phasor approach analysis of multiphoton FLIM measurements to probe the metabolic activity of three-dimensional in vitro cell culture models," Sci. Rep. **7**(1), 42730–11 (2017).
35. L. Malacrida, S. Ranjit, D. M. Jameson, *et al.*, "The Phasor Plot: A Universal Circle to Advance Fluorescence Lifetime Analysis and Interpretation," Annu. Rev. Biophys. **50**(1), 575–593 (2021).
36. B. K. Wright, L. M. Andrews, J. Markham, *et al.*, "NADH distribution in live progenitor stem cells by phasor-fluorescence lifetime image microscopy," Biophys. J. **103**(1), L7–L9 (2012).
37. J. L. Lagarto, M. B. Nickdel, D. J. Kelly, *et al.*, "Autofluorescence Lifetime Reports Cartilage Damage in Osteoarthritis," Sci. Rep. **10**(1), 2154 (2020).
38. W. Becker, *The bh TCSPC Handbook*, Scanning (800), 1–566 (2010).
39. W. Becker Editor, *Springer Series in Chemical Physics 111 Advanced Time-Correlated Single Photon Counting Applications* (n.d.).
40. A. J. Walsh, R. S. Cook, H. C. Manning, *et al.*, "Optical metabolic imaging identifies glycolytic levels, subtypes, and early-treatment response in breast cancer," Cancer Res **73**(20), 6164–6174 (2013).
41. A. T. Shah, K. E. Diggins, A. J. Walsh, *et al.*, "In Vivo Autofluorescence Imaging of Tumor Heterogeneity in Response to Treatment," Neoplasia **17**(12), 862–870 (2015).
42. L. Reinsalu, M. Puurand, V. Chekulayev, *et al.*, "Energy metabolic plasticity of colorectal cancer cells as a determinant of tumor growth and metastasis," Front. Oncol. **11**, 698951 (2021).
43. Z. C. Nwosu, D. A. Megger, S. Hammad, *et al.*, "Identification of the consistently altered metabolic targets in human hepatocellular carcinoma," Cell. Mol. Gastroenterol. Hepatol. **4**(2), 303–323.e1 (2017).
44. Q. Huang, Y. Tan, P. Yin, *et al.*, "Metabolic characterization of hepatocellular carcinoma using nontargeted tissue metabolomics," Cancer Res **73**(16), 4992–5002 (2013).